



Full length article

Changes in local surface structure and Sr depletion in Fe-implanted SrTiO₃ (001)O. Lobacheva ^{a,*}, Y.M. Yiu ^b, N. Chen ^c, T.K. Sham ^{a,b}, L.V. Goncharova ^{a,b}^a Department of Physics and Astronomy, Western University, London, ON N6A 5B7, Canada^b Department of Chemistry, Western University, London, ON N6A 5B7, Canada^c Canadian Light Source, Saskatoon, SK S7N 0X4, Canada

ARTICLE INFO

Article history:

Received 20 April 2016

Received in revised form

21 September 2016

Accepted 25 September 2016

Available online 26 September 2016

Keywords:

XPS

XANES

Fe-doped SrTiO₃

Ion implantation

ABSTRACT

Local surface structure of single crystal strontium titanate SrTiO₃ (001) samples implanted with Fe in the range of concentrations between 2×10^{14} to 2×10^{16} Fe/cm² at 30 keV has been investigated. In order to facilitate Fe substitution (doping), implanted samples were annealed in oxygen at 350 °C. Sr depletion was observed from the near-surface layers impacted by the ion-implantation process, as revealed by Rutherford Backscattering Spectrometry (RBS), X-ray photoelectron spectroscopy (XPS), X-ray Absorption Near Edge Spectroscopy (XANES), and Atomic Force Microscopy (AFM). Hydrocarbon contaminations on the surface may contribute to the mechanisms of Sr depletion, which have important implications for Sr(Ti_{1-x}Fe_x)O_{3-δ} materials in gas sensing applications.

© 2016 Elsevier B.V. All rights reserved.

1. Introduction

Strontium titanates among other perovskite oxides have recently attracted significant attention due to their outstanding electrical and ionic transport properties [1,2]. Pure SrTiO₃ (or STO) is a wide band semiconductor with an indirect band gap of 3.25 eV and a direct band gap of 3.75 eV with low conductivity. Substitution of Ti by another transition metal, such as Fe, can change the electronic structure and electrical conductivity of the oxide. Various titanates, including SrTi_{1-x}Fe_xO_{3-δ}, are considered as promising inexpensive alternative to the classical oxygen sensors based on zirconia [1], especially for use in harsh environments.

SrTi_{1-x}Fe_xO_{3-δ} oxides form a family of continuous solid solutions in the range $0 < x < 1$ from strontium titanate to strontium ferrate. With variation of x , properties of SrTi_{1-x}Fe_xO_{3-δ} change from large band gap semiconductor for Ti-rich phase to a conductor for Fe-rich phase (for $x > 0.1$) [3,4]. SrTiO₃ has cubic perovskite structure. On the other hand, SrFeO_{3-δ} forms different crystal phases from disordered perovskite SrFeO₃ to ordered brownmillerite SrFeO_{2.5} [5,6]. Mixed compound SrTi_{1-x}Fe_xO_{3-δ} can retain cubic perovskite structure in wide range of x [6,7].

Fe in Ti⁴⁺ site can acquire two different oxidation states, Fe³⁺ and Fe⁴⁺. The difference in the oxidation state requires oxygen vacancies to be an integral part of the perfect SrTi_{1-x}Fe_xO_{3-δ} lattice to keep charge neutrality. If one uses the stoichiometry of SrTi_{1-x}Fe_xO_{3-x/2} [6,8], then half of the Fe³⁺ can have a mobile oxygen vacancy with an effective positive charge +2 (or V_O^{**} using Kröger–Vink notation [9]). There are three types of coordination around oxygen sites: (i) Fe—O—Fe; (ii) Ti—O—Ti; and (iii) Ti—O—Fe. Iron can be in 4-, 5-, and 6-coordination in SrTi_{1-x}Fe_xO_{3-δ} with different defect energies of the oxygen vacancies corresponding to these configurations [10]. The Fe³⁺/Fe⁴⁺ ratio will depend on the total Fe concentration x , the oxygen partial pressure $p(O_2)$ and the temperature. For $x \approx 0.1$ –0.3, the electrical resistivity stays almost constant in the $p(O_2)$ range of 10^{-4} –1 bar in the temperature range 750–1000 °C, which is suitable for oxygen sensor applications [6]. Presence of Fe doping and accompanying oxygen vacancies also enhances surface reactivity of strontium titanate [3,11–13]. The good conductivity, both ionic and electronic, in combination with chemical and structural stability makes Fe-doped STO an attractive material for applications in gas sensors [1,2,14], catalysts [15], fuel cell electrodes [16,17], oxygen permeation membrane [3,18] and resistive switching memory [19–21].

A number of studies have suggested that Fe substitutes Ti due to close ionic radius and valence state. However the substitution of Sr by a dopant transition metal has also been explored. Both experimental and theoretical research on Mn-doped SrTiO₃ powders have

* Corresponding author.

E-mail address: olobache@gmail.com (O. Lobacheva).

indicated that Mn can occupy either Ti (as Mn^{4+}) or Sr site (as Mn^{2+}) depending on the experimental conditions (temperature, oxygen partial pressure and stoichiometry) [22–24]. The calculations performed by Yang et al. [23] have shown that Mn substitution on Ti site is explicitly preferable only in oxygen rich conditions, whereas in oxygen deficit conditions Mn prefers to substitute Sr site.

In this work, ion beam implantation was employed for Fe doping of STO single crystals. The method allows us to introduce doping in a controllable way by varying the incident ion energy and concentrations. Here we have chosen Fe implantation doses to result in final Fe concentrations below the solubility level of Fe in the host STO material. For Fe doses above $\sim 1 \times 10^{17}$ atoms/cm², there is a possibility to form metallic Fe nanoparticles inside the host material [25–27]. For instance, Dulov et al. [25] reported the formation of α -Fe nanoparticles in $SrTiO_3$ at the implantation dose of 1.5×10^{17} ions/cm², whereas at the dose of 0.75×10^{17} ions/cm², they mostly observed formation of $SrTi_{1-x}Fe_xO_{3-\delta}$ phase. Therefore, smaller implantation doses were used in this study to avoid precipitation of iron.

Using Rutherford backscattering spectrometry (RBS), we observe an unusual depletion or apparent loss of Sr during implantation and post-implantation annealing at high temperatures in oxygen environment. Sr depletion is correlated with the Fe dose and most noticeable at the highest implantation doses and after 350 °C annealing. Typical losses of the low Z elements such as Ti, and O due to preferential sputtering effects are not noticeable at our experimental conditions. Local chemical environment of the implanted and annealed samples were evaluated with X-ray photoemission spectroscopy (XPS) and X-ray absorption near edge structure (XANES) spectroscopy. While XPS allows us to monitor changes on the surface, XANES gives us additional information about structural changes within the whole layer thickness affected by implantation. Due to the chemical selectivity of X-ray absorption spectroscopy, we can characterize the local surrounding of Ti and Fe atoms independently. XANES is particularly suitable to study ion-irradiated systems, which can be disordered since no long range crystal order is necessary to get this information. Possible mechanisms of the decomposition of near-surface $SrTi_{1-x}Fe_xO_{3-x/2}$ layer into $SrCO_3$, SrO or $Sr(OH)_2$, and TiO_2 are proposed and explained from thermodynamics arguments.

2. Experimental details

Strontium titanate single crystal substrates ($SrTiO_3$ (001), $5 \times 5 \times 0.5$ mm³ with both face polished) were purchased from MTI Crystals, Inc. (USA). Fe was implanted at controlled room temperature, incident energy 30 keV, 7° off normal to avoid channeling, at vacuum of 5×10^{-8} Torr at the Tandetron facility, Western University, Canada. The $SrTiO_3$ substrates were implanted with iron at doses of 2×10^{14} , 8×10^{14} , 1×10^{16} and 2×10^{16} Fe ion/cm² (samples henceforth denoted STO-Fe2e14, STO-Fe8e14, STO-Fe1e16 and STO-Fe2e16, respectively). To heal irradiation damage implanted samples were annealed for 2 h at 350 °C in O_2 atmosphere (samples STO-Fe2e14-350, STO-Fe8e14-350, STO-Fe1e16-350 and STO-Fe2e16-350, respectively). Though most of results presented below are related to the STO samples with the highest implantation dose (2×10^{16} Fe ion/cm²), the samples with lower doses were also analyzed to monitor the influence of implantation doses.

Rutherford Backscattering Spectrometry (RBS) measurements were conducted using 500 keV He⁺ beams in random and channeling geometries, at Tandetron facility. RBS was performed in several spots on the surface to confirm the uniformity of the implantation process and composition, with a Si charged particle detector at 170°. An Sb-implanted amorphous silicon sample with a known

total Sb content of 4.82×10^{15} atoms/cm² was used to calibrate the detector solid angle. RBS data were fitted using SIMNRA [28] to determine elemental composition and stoichiometry.

X-ray photoelectron spectroscopy (XPS) analysis of STO samples were performed at Surface Science Western at the University of Western Ontario with a Kratos Axis Ultra spectrometer, with a monochromatic Al K α source (15 mA, 14 kV) at photon energy of 1486.7 eV. Instrument pressure during the spectra acquisition was better than 8×10^{-10} Torr. The Kratos charge neutralizer system was used with spectral correction by monitoring C 1s peak which was set to 285.0 eV. High-resolution spectra were obtained using an analysis area of $\sim 300 \mu m \times 700 \mu m$ and either a 10 eV or 20 eV pass energy which corresponding to Ag 3d_{5/2} FWHM of 0.47 eV and 0.55 eV, respectively [29–31]. In order to perform depth resolved analysis, surface of the samples was sputtered with Ar⁺ ion beam. Sputter rates were calculated based on an Al_2O_3/Al standard (1.32 nm/min). Analyses were carried out on the surface and at 10, 20, 30 and 40 nm depths on virgin STO, Fe-implanted STO-Fe2e16 and implanted and annealed STO-Fe2e16-350C samples. XPS spectra were fitted using CasaXPS software [32].

X-ray Absorption Near Edge Spectroscopy (XANES) was used to identify the chemical environment of Ti and Fe in STO. Fe L-edge XANES experiments were performed at the Canadian Light Source (CLS) (Saskatoon, Canada) at the high resolution Spherical Grating Monochromator (SGM) beamline which uses a 45 mm planar undulator and three gratings covering an X-ray photon energy range from 250 to 2000 eV. It provides resolution greater than 5000 E/ΔE at energy below 1500 eV and better than 10000 E/ΔE at the N K-edge. The photon energy was calibrated at C K-edge at 284.2 eV. Fe K-edge spectra were measured at the Advanced Photon Source (APS) at Argonne National Laboratory (Argonne, IL, USA) at the CLS@APS on the PNC/XSD beamline (20-BM). The beamline uses Si double-crystal monochromator to cover a photon energy range of 5 to 25 keV and offers resolution greater than 7000 E/ΔE. The double-crystal monochromator photon energy was calibrated at the Fe K-edge threshold of a Fe foil at 7110.6 eV.

The absorption spectra were collected in total fluorescence yield (TFY) and total electron yield (TEY) at the CLS. TEY is more surface sensitive than TFY due to the short escape depth of electrons in matter. Simultaneous collection of TEY and TFY absorption spectra allows discerning bulk and surface signal, respectively, in XANES of STO samples. However, significant charging of STO samples during acquisition caused distortion in XANES spectra collected in TEY mode in some cases, and are not shown.

XANES spectra were normalized to the intensity of the incident beam I_0 , measured as the current emitted from a gold mesh simultaneously with spectrum acquisition. Continuous background was subtracted from data as an extrapolated linear curve fitted in the pre-edge area. For a consistent data analysis, spectra were normalized to unity above absorption edge. In some cases it was impractical, and the spectra were normalized to unity by the intensity of the first sharp intense peak (traditionally referred as a “white line”).

The EXAFS spectra have been analyzed using the software program Athena. The backgrounds have been removed with E_0 set at 7126 eV with k weight at 2. The Hanning window was used for the forward and backward Fourier Transform. The forward Fourier transforms had the k-range set at 3.0–18 and k weight at 0.5. The backward Fourier transforms had the R-range set at 1–3. The Real Space Multiple Scattering program (FEFF9) was used to simulate spectra of the proposed cluster structures consisting of 173 atoms with $Pm\bar{3}m$ group symmetry [33,34]. With full multiple scattering, the simulation paths are cut to a cluster of 15 atoms. Starting from the initial stoichiometric structure, some of Ti and Sr ions were replaced by Fe atoms without significant changes in interatomic

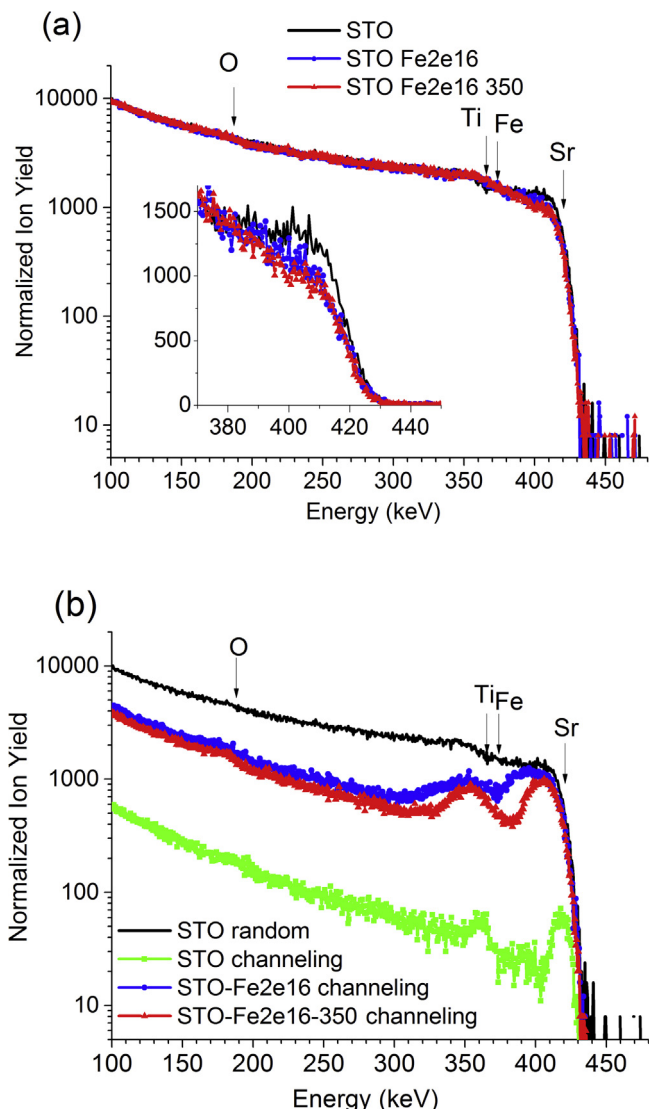


Fig. 1. (a) RBS spectra of STO, STO-Fe2e16 and STO-Fe2e16-350 samples collected in random geometry, 7° off normal, 500 keV He^+ incident beam. (b) RBS spectra of STO, STO-Fe2e16 and STO-Fe2e16-350 samples collected in channeling geometry; RBS random spectrum of STO crystal is shown for comparison.

distances. Furthermore, to account for oxygen vacancies within the cluster, some specified fractions of the first-shell oxygen atom was removed, counting from incorporated Fe.

Atomic force microscopy (AFM) topography images were recorded using Multimode AFM with Nanoscope IIIA controller (Digital Instruments) using a scanner with a maximum lateral motion of $\sim 12 \mu\text{m}$ and silicon nitride cantilevers. Imaging was performed in contact mode at ambient temperature at scan rates of 2–27 Hz.

3. Results

RBS spectra collected in random geometry for STO, STO-Fe2e16 and STO-Fe2e16-350 samples are presented in Fig. 1(a). Positions of the Sr, Ti, Fe and O surface peak are marked with arrows. A closer analysis of Sr signal at the energies of 370–420 keV, reveals a noticeable decrease in Sr areal density in the near-surface region (inset in Fig. 1(a)). Compared to the reference STO sample, the sample implanted with the highest dose lost $\sim 8.6\%$ of Sr following implantation (sample STO-Fe2e16), and $\sim 10.8\%$ of Sr, following Fe implantation and annealing (sample STO-Fe2e16-350), which is

Table 1

Integrated areal densities for Sr peak (energy range of 370–420 keV) in RBS spectra for samples implanted with Fe at different doses, before and after crystallization anneal.

Fe dose, $\times 10^{16}$ atoms/cm ²	Sr peak reduction after implantation, %	Sr peak reduction after implantation and anneal, %
1.0	7.0 ± 0.4	10.2 ± 0.5
2.0	8.6 ± 0.4	10.8 ± 0.5

substantially larger than the uncertainty of RBS method. The effect was also detected in the samples with lower implantation dose STO-Fe2e16 and STO-Fe2e16-350. This decrease in Sr ion yields for near-surface region was quantified and summarized in Table 1. The results show that this effect depended on the implantation dose. It was much less pronounced on the samples implanted with 2×10^{14} and 8×10^{14} Fe^+/cm^2 .

RBS spectra collected in channeling geometry allowed us to estimate the crystallinity of the initial STO crystal and irradiation damage due to ion implantation (Fig. 1(b)). In the channeling geometry, the ion yield is greatly reduced if subsurface atoms are in their ideal lattice positions. However atoms in disordered regions and amorphous regions will be visible to the ion beam. Thus, the degree of crystallinity of the samples can be determined by taking the ratio of the yield in the channeling geometry to a random direction yield (“the maximum yield”). RBS spectra along the [001] axis (Fig. 1(b)) reveal that this ratio is close to $\sim 6 \pm 1\%$ for the virgin STO crystal which proves good crystalline order of the initial STO before implantation. Distinct peaks of strontium, titanium and oxygen can be observed corresponding to the top surface layer of the STO sample. After Fe implantation, there is a systematic increase in the detected ion yields for the implanted samples (STO-Fe2e16), both in the top-surface layer yields, and in the bulk of the STO sample. Crystallinity of the samples is improved after annealing in oxygen, though it does not reach the initial (prior-to-implantation) values (Fig. 1(b)).

High-resolution XPS spectra for Sr 3d, Ti 2p, O 1s and C 1s peaks are presented in Fig. 2 for the STO samples with the highest implantation dose, before and after recrystallization annealing. Data for the initial STO crystals (before implantation) are given as a reference.

A significant decrease in Sr peak intensities is noticeable in the Sr 3d XPS spectra of the STO samples after implantation and annealing (Fig. 2(a)), which is consistent with our RBS results. Sr 3d peaks of virgin STO were fitted with $\text{Sr } 3d_{3/2}$ and $\text{Sr } 3d_{5/2}$ peak components as shown in Fig. 2(a). However Sr 3d spectra of STO-Fe2e16 and STO-Fe2e16-350 samples were fitted by two Gaussians doublets separated by ~ 0.9 eV. The presence of high binding energy (HBE) contributions in the spectra shows that Sr exists in two different chemical environments on the surface in these samples.

XPS Ti 2p spectra of the STO samples are presented in Fig. 2(b). The $\text{Ti } 2p_{3/2}$ and $\text{Ti } 2p_{1/2}$ peaks are located at 458.1 eV and 463.82 eV (Fig. 2(b)), respectively, for all samples, consistent with the reported values for Ti^{4+} state [31]. The peak positions and the line splitting are in good agreement with the values reported for SrTiO_3 in the literature [35,36]. At the same time, there is a notable decrease in peaks intensities following implantation (Fig. 2(b)).

The peaks at 529.2 eV, 530.9 eV and 532.0 eV were discerned in the O 1s spectra of STO samples (Fig. 2(c)). The peak at ~ 529.2 eV was identified as the chemical state of oxygen in SrTiO_3 lattice, and the other two peaks, at higher binding energies were ascribed to hydroxide and/or defective oxides (530.9 eV) and to water and/or organic compounds on the surface carbonate form (532.0 eV) [31,37].

The data from C 1s spectra show a similar trend (Fig. 2(d)) as observed with O 1s peaks. The chemical states of carbon were iden-

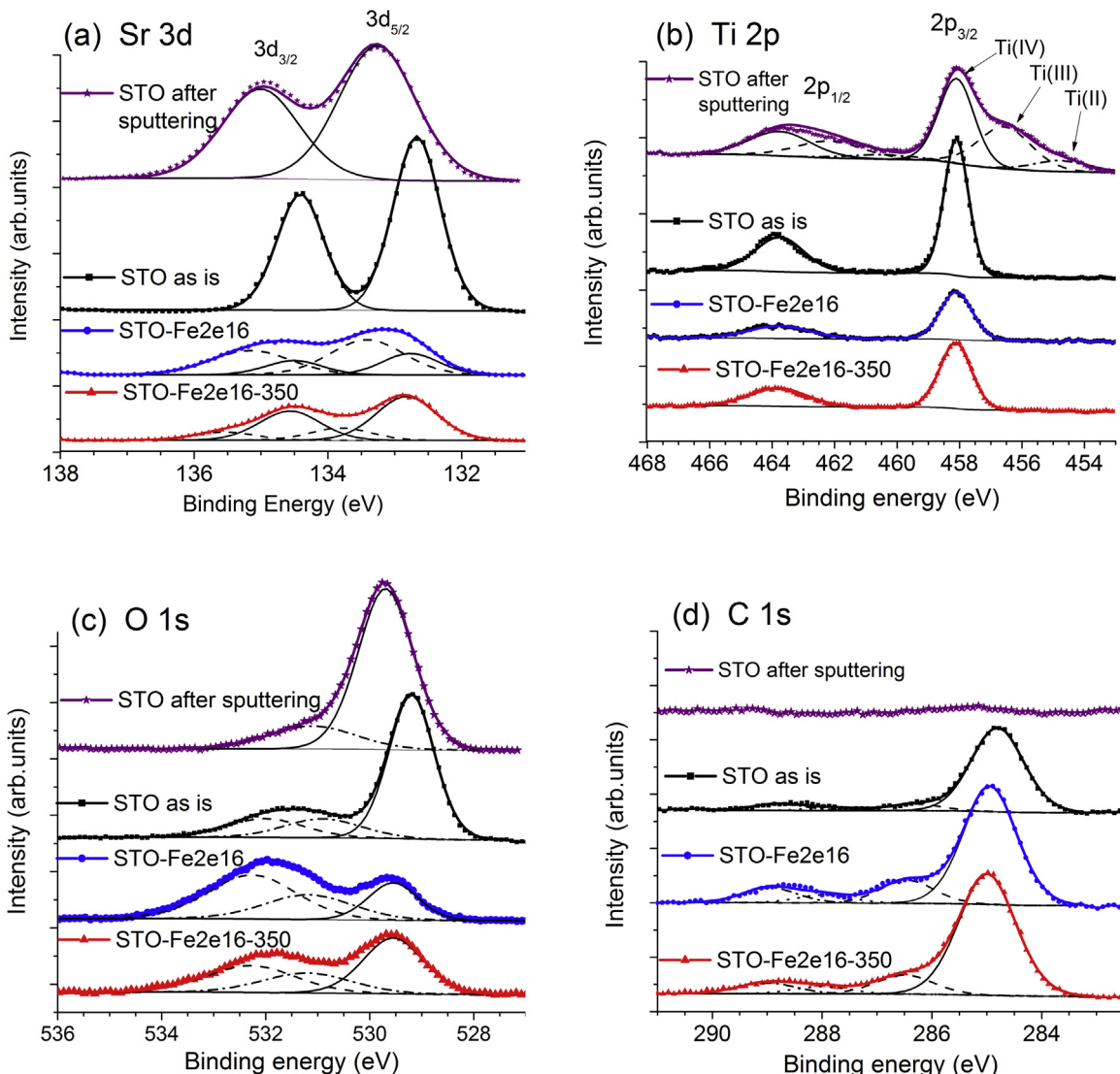


Fig. 2. XPS spectra: (a) Sr 3d; (b) Ti 2p; (c) O 1s; (d) C 1s peaks for STO (black squares), STO-Fe2e16 (blue circles), STO-Fe2e16-350 (red triangles) and STO after sputtering of 10 nm layer (purple stars). (For interpretation of the references to colour in this figure legend, the reader is referred to the web version of this article.)

tified as the carbon in C–CH_x and the carbonate form. The position of the peaks indicated the possible formation of alcohol (C–OH) and/or ether (C–O–C), carbonyl (C=O) and carboxyl (O=C=O) functional groups. The carbonate peak increases after implantation, while C–C peak decreases. As it can be noticed from O 1s and C 1s spectra, the thermal treatment changed the amount of different functional groups but did not remove them completely.

Because there have been no difference noticed between the Ti 2p, Sr 3d, O 1s and C 1s spectra of the STO samples at any sputtered depth, Fig. 2 presents only spectra of STO crystal after sputtering of 10 nm layer. Positions of peaks in XPS spectra are summarized in Table 2. As expected, Ar sputtering introduced considerable damage to the STO surface. Thus, there was preferable sputtering of O and C, which has left the surface in oxygen depleted conditions.

All sputtered samples presented a noticeable chemical shifts to higher binding energy in the main components of Sr 3d peaks in spectra of implanted and sputtered samples (Fig. 2(a)). Ar sputtering, done in the high vacuum inside the XPS apparatus, has efficiently removed almost all the traces of water molecules and carbon-containing contaminations disappear from the XPS spectra. O 1s spectra collected from the sputtered samples show no contributions from hydroxide (water) (Fig. 2(c)). O 1s peak from

oxygen in strontium titanate structure becomes more intensive. As sputtering removes organic compounds from the sample surface the intensity of C 1s drops to the noise level for all sputtered STO samples (Fig. 2(d)).

Due to preferential sputtering of oxygen, XPS spectra did not show the correct oxidation states of elements in the bulk of STO. As could be seen from Ti 2p peaks after sputtering up to 50% of Ti were reduced from Ti⁴⁺ to Ti³⁺ and Ti²⁺ (Fig. 2(b)). For the same reason the oxidation state of implanted Fe was Fe⁰ as identified from Fe 2p XPS peaks (Fig. 3(a)) in both Fe implanted and oxygen annealed samples, STO-Fe2e16 and STO-Fe2e16-350.

No Fe was detected in XPS spectra of STO-Fe2e16 and STO-Fe2e16-350 collected at the surface before sputtering. The step-by-step sputtering of STO-Fe2e16 surface showed that Fe could be found in the 40 nm deep layer (Fig. 3). The distribution of implanted Fe calculated from the peaks intensity with maximum is in excellent agreement with SRIM prediction showing a maximum at 20 nm depth (Fig. 3(b)). Annealing at 350 °C did not lead to any significant diffusion of the implanted Fe.

The oxidation state of Fe in STO samples was established using XANES Fe L-edge spectra (Fig. 4(a)). The Fe L-edge spectrum was collected in TEY and TFY modes. Two single peaks at ~709.0 eV and

Table 2

Experimental positions of XPS peaks (eV) in spectra of STO samples implanted with 2×10^{16} Fe⁺ ions/cm² before and after crystallization anneal.

Sample	STO	STO-Fe2e16	STO-Fe2e16-350C	STO-sputtered ^a
Sr(II) 3d _{5/2}	132.67	133.06	132.80	133.30
Sr(II) 3d _{5/2} (HBE) ^b	–	133.96	133.70	–
Sr(II) 3d _{3/2}	134.41	134.81	134.55	135.00
Sr(II) 3d _{3/2} (HBE) ^b	–	135.71	135.45	–
Ti(IV) 2p _{3/2}	458.10	458.10	458.10	458.10
Ti(IV) 2p _{1/2}	463.84	463.84	463.84	463.84
Ti(III) 2p _{3/2}	–	–	–	456.70
Ti(III) 2p _{1/2}	–	–	–	462.43
Ti(II) 2p _{3/2}	–	–	–	455.00
Ti(II) 2p _{1/2}	–	–	–	460.58
O 1s (due to oxide)	529.20	529.56	529.55	529.71
O 1s (due to hydroxide, defective oxide)	530.90	531.19	531.20	531.12
O 1s (due to water, organic oxygen)	532.06	532.28	532.28	–
C 1s (due to C—C, C—H)	284.80	284.94	284.99	–
C 1s (due to C—OH, C—O—V)	286.29	286.46	286.50	–
C 1s (due to C=O)	287.75	287.93	287.99	–
C 1s (due to C—O—H)	288.80	288.94	289.00	–

^a After sputtering XPS spectra of all analyzed STO samples were identical at all sputtering depth.

^b High binding energy (HBE) component is present in Sr 3d XPS spectra of STO-Fe2e16 and STO-Fe2e16-350C.

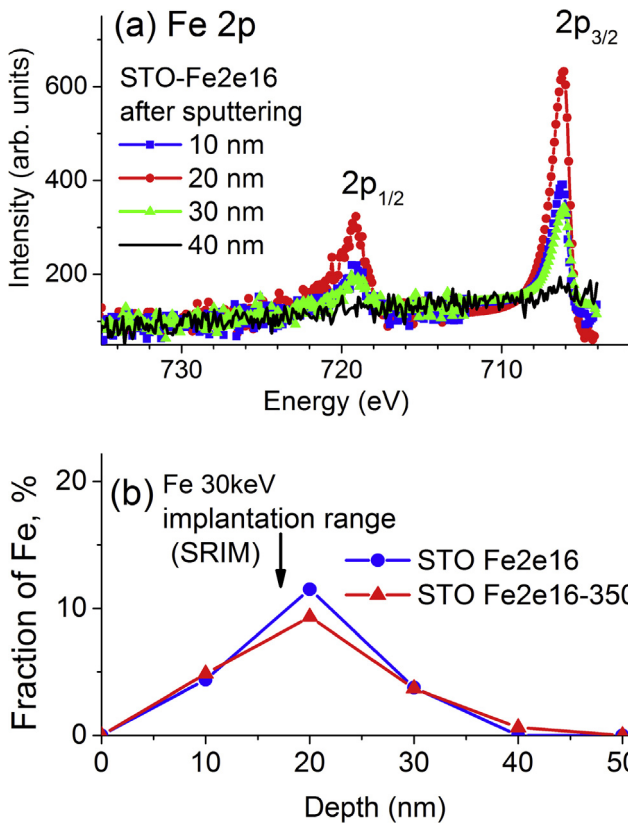


Fig. 3. XPS sputtering results: (a) Fe 2p peaks on after sputtering of STO-Fe2e16 to different depths; (b) distribution of Fe as a function of depth in STO-Fe2e16 and STO-Fe2e16-350.

~722.0 eV were observed in TEY and TFY XANES spectra of STO-Fe2e16 sample (Fig. 4(a)). The shape of the spectra shows that iron is in Fe⁰ oxidation state throughout the implanted area. In XANES spectra of STO-Fe2e16-350, the peaks became doublets (with separation of ~1.7 eV) indicating formation of Fe oxide. The ratio of intensities of peaks within the doublets differs in TEY and TFY XANES spectra (Fig. 4(a)). The difference allowed us to identify that iron oxidation state was Fe³⁺ in bulk and Fe²⁺ in near-surface area.

The findings were confirmed by Fe K-edge XANES analysis (Fig. 4(b)). A shoulder at ~7112 eV in the pre-edge region of STO-Fe2e16 spectrum implies metallic state of iron Fe⁰. The spectrum of Fe foil is shown in Fig. 4(b) for comparison. However the spectrum

Table 3

The values of average roughness R_a evaluated for specific profiles of the STO samples surface.

Sample	Roughness, R _a , nm (5 μm scan dimensions)
STO	0.32 ± 0.06 nm
STO-Fe2e16	0.45 ± 0.09 nm
STO-Fe2e16-350	0.77 ± 0.14 nm

of the STO-Fe2e16-350 has a sharp pre-edge peak at ~7113 eV, which is typical for oxidized iron. The broadening and disappearance of the oscillations above the absorption edge strongly suggest that implanted iron does not have long-range order but only short-range order in these samples.

Fig. 5 presents results of Fourier Transform of EXAFS for STO-Fe2e16-350 sample and FEFF simulations for several models. We expected Fe to substitute on either Ti or Sr site, and this substitution is accompanied by formation of oxygen vacancies to compensate charge. To simulate the effect of oxygen vacancies, the oxygen ions from the nearest shell were removed. In this manner six models were used for clusters where Fe substitutes on either Ti or Sr site, and 1/3, 2/3 and 3/3 of oxygen removed from the nearest shell. Comparison of FT of experimental EXAFS and simulations data (Fig. 5) showed the model where Fe substitutes on Sr site and 1/3 of oxygen in nearest shell is removed has the best agreement with experimental results. The placing of Fe ion on the vacant Ti site produced poorer approximation or required more oxygen vacancies at the nearby oxygen shells to obtain equally good fit.

Results of AFM analysis performed on STO samples to trace changes in surface topography before and after ion implantation are displayed in Fig. 6. Ambient AFM images of STO samples before and after implantation demonstrate stepped topography with average roughness close to single step heights reported for STO single crystals [38]. Values of average roughness, R_a, measured for specific profiles of STO samples are listed in Table 3. Roughness does not change significantly after Fe implantation; however it increases after post-implantation annealing, which indicates partial decomposition of the top surface layer. A similar behavior was also observed in AFM images reported by Lee et al. [38] for SrRuO₃ films on STO substrates.

4. Discussion

Ion irradiation creates defects leading to an increased reactivity of strontium titanate surface [13,39]. Surface defects were identified as active sites for reaction of CO, CO₂ and H₂O with STO surface

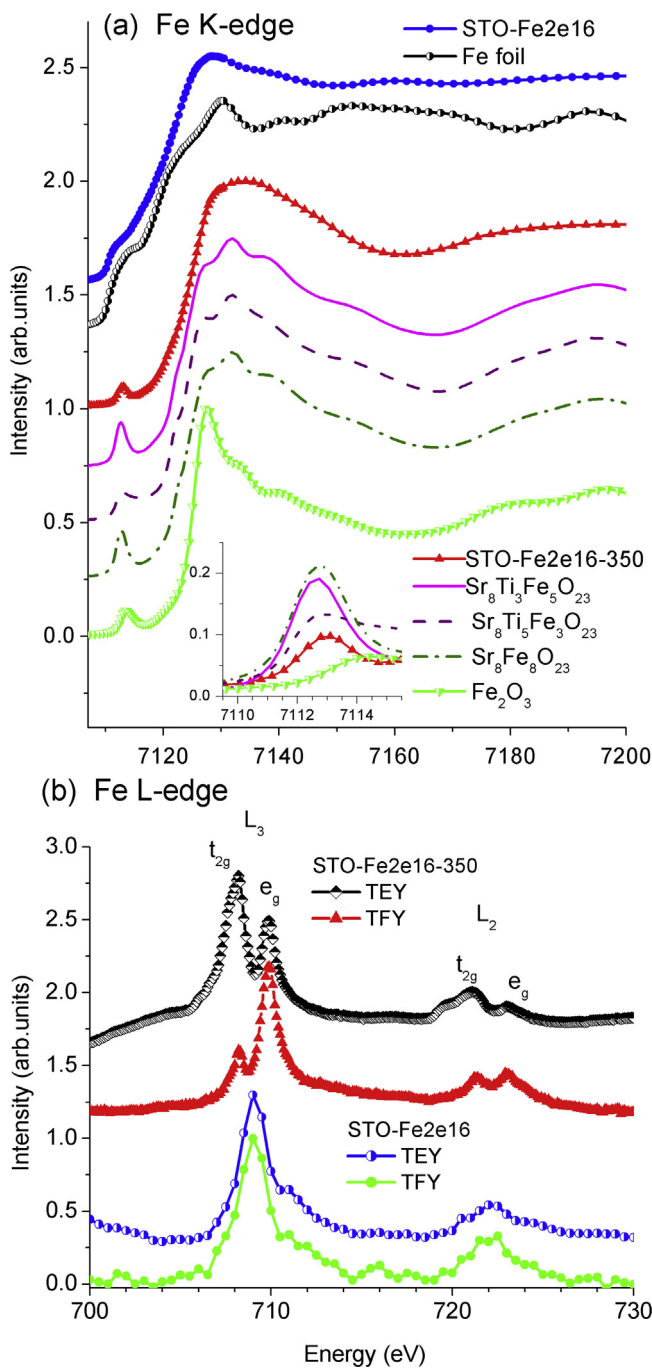


Fig. 4. (a) XANES Fe K-edge of STO-Fe2e16 and STO-Fe2e16-350 samples, Fe foil and Fe_2O_3 , and results of FEFF9 simulation for $\text{Sr}_8\text{Fe}_8\text{O}_{23}$, $\text{Sr}_8\text{Ti}_5\text{Fe}_3\text{O}_{23}$ and $\text{Sr}_8\text{Ti}_3\text{Fe}_5\text{O}_{23}$; (b) XANES Fe L-edge of STO-Fe2e16 and STO-Fe2e16-350 samples, collected in TFY (solid symbols) and TEY (semi-open symbols) mode.

[11–13]. For instance, it was shown that defect-free pure SrTiO_3 (100) surfaces do not interact with water at temperatures below 200 K. However H_2O readily adsorbs on the SrTiO_3 surface defects created by sputtering [11].

We observe formation of different carbon and oxygen groups due to exposure to the ambient atmosphere and this leads to the increase of the intensity of XPS O 1s and C 1s peaks. The implanted and annealed STO-Fe2e16-350C had less intensive water/organic oxygen since it was annealed in oxygen. C peak is higher for the STO-Fe2e16 and STO-Fe2e16-350C compared to the virgin STO crystal due to a large number of defects on the surface of implanted sam-

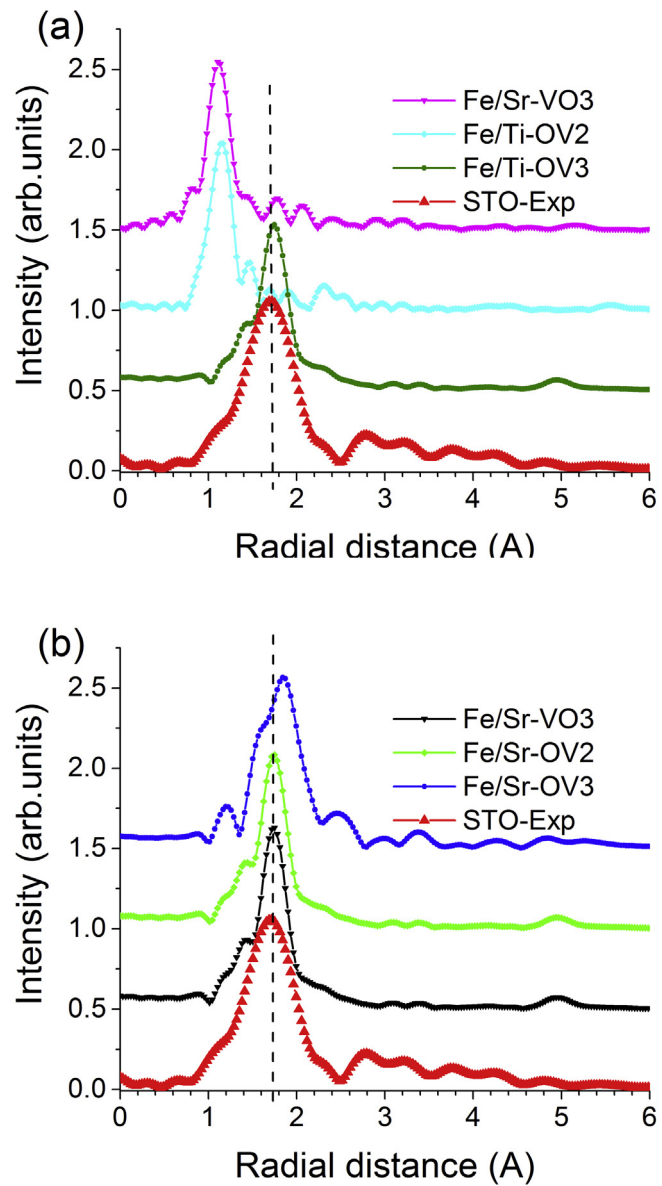


Fig. 5. Fourier Transform of experimental EXAFS for STO-Fe2e16-350 sample and FFF9 simulations for several proposed models: (a) for Fe substituting Ti center, and (b) for Fe substituting Sr center. The numbers of created O vacancies within the first shell from are designated by OV1-3, where OV1 corresponds to one vacancy.

ples. It is likely that the surface reactions have led to dissociation of the molecules with further formation of SrCO_3 .

Depending on the samples treatment, the Sr 3d peak shift has been ascribed to hydroxyl species $\text{Sr}-\text{COH}$ [36,41], SrO_x layers [41] or strontium carbonate SrCO_3 , formed due to reaction of STO surface with CO and CO_2 [36,37]. Pilleux et al. [35] have observed the Sr 3d peak shifts from 132.7 eV for as-grown STO films on Ti foil to 133.0 eV for Ar sputtered surface. The authors explained their observation by the presence of hydroxyl groups absorbed on the surface prior to Ar ion irradiation. In more recent study of $\text{SrTiO}_3(001)$ surface, the Sr peak shift was explained by a change in the Madelung potential due to oxygen vacancies formed by ion irradiation [40]. With the decrease of the coordination number of a metal atom, the electrostatic potential of the cationic sites diminishes and the atomic screening of the core hole increases. In principle, these effects should effectively decrease the binding energy in the metal atom. However Van der Heide et al. [40] detected an increase of the Sr 3d binding energy in Ar sputtered

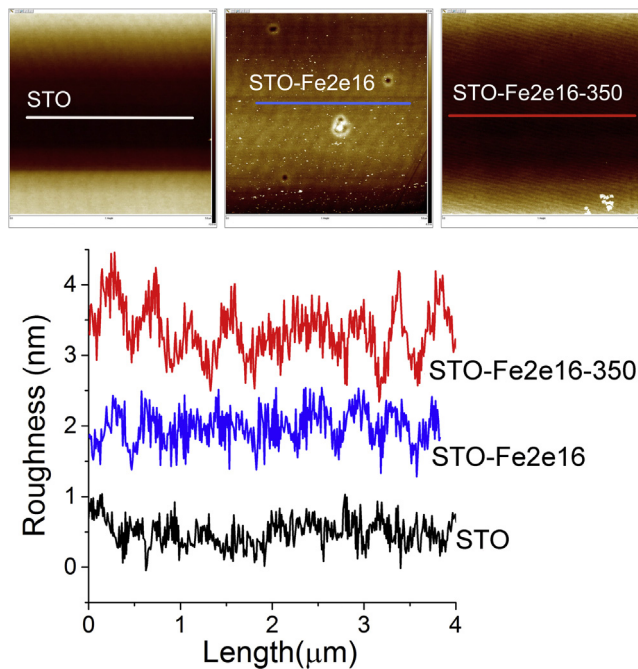


Fig. 6. AFM images and topography scans of strontium titanate single crystals before ion implantation (STO), after implantation (STO-Fe2e16) and after implantation and anneal (STO-Fe2e16-350) registered in air.

STO samples. They explained their observation by the decrease of the negative Madelung potential at the cationic sites (an initial-state effect) as well as decrease of the polarization screening (a final-state effect) when the coordination number of a metal atom become lower. These processes increase the binding energy in the metal atom [40].

These considerations can explain our experimentally observed increase of the Sr binding energy in Fe-implanted STO crystal and, likewise, the presence of Sr 3d doublets in the spectrum of implanted and annealed samples. The appearance of HBE components in STO-Fe2e16 and STO-Fe2e16-350 Sr 3d spectra can be ascribed to SrCO_3 formed due to reactions with CO and CO_2 on STO surface [38,40], while shift of the main component of Sr 3d peaks to the higher binding energy can be explained by the decrease of the Madelung potential (see Table 2).

There have been reports of the surface instability and phase separation under influence of ion and electron irradiation and thermal treatment [42–44]. Moreover, some studies have shown possible Sr segregation, either as SrO or Sr excess phases $\text{SrO}\text{-n}(\text{SrTiO}_3)$ [43,44]. For instance, Sabathier et al. [43] have identified Sr_2TiO_4 and TiO_2 phase separation induced by 320 keV Pb^{2+} ions irradiation. Shin et al. [42] have observed SrRuO_3 surface decomposition during annealing in vacuum at 200–800 °C temperature range. Same authors [42] have emphasized the role of hydrocarbon contaminations as one of conditions for SrRuO_3 surface roughening and decomposition on SrO and Ru phases. SrO desorption during low (<500 °C) temperature annealing can be another reason for Sr depletion during our recrystallization conditions. For example, SrO desorption was observed by Goncharova et al. [45] in epitaxial $\text{SrTiO}_3/\text{Si}(001)$ films with a desorption peak at ~450 °C.

The Sr depletion in Fe implanted STO observed in our present experiment can be partly related to relative decrease of Sr content in the result of the formation of the adsorbate layer on the STO surface. XPS analysis suggested formation of strontium carbonate and strontium hydroxide on the STO surfaces after Fe ion irradiation. Both SrCO_3 and Sr(OH)_2 have lower density compared to SrTiO_3 . As a result, the surface layer of STO-Fe2e16 and STO-Fe2e16-350

(in RBS analysis) is seen as Sr deficient. At the same time, as followed from AFM images, the average roughness of STO surface increased after Fe irradiation and post-implantation annealing, which also can be an indication of transformations in the surface area.

The dependence of Sr apparent loss on the implantation dose, noticed in RBS spectra, can be correlated with the different concentration of defects produced during ion irradiation. SRIM simulation showed that ion irradiation led to disordering and formation of oxygen vacancy defects in STO crystal. Formation of Sr vacancies/interstitials is also possible in Fe implanted STO crystals though in much lower concentration than oxygen vacancies. The Sr depleted layer was much thicker than the probing depth of XPS. As evident from the results of RBS depth profile analysis, the changes in Sr content were not limited by the surface area, but affected the entire implantation depth. So, Sr depletion cannot be explained entirely by the formation of different surface phase only.

XANES analysis conducted at Fe L-edge in this work showed the change of Fe oxidation state from Fe^0 in as-implanted STO to Fe^{3+} and Fe^{2+} in the implanted and oxygen annealed STO samples. The result does not comply with the previous studies conducted on $\text{SrTi}_{1-x}\text{Fe}_x\text{O}_{3-\delta}$ powders which have suggested that Fe can substitute for Ti in STO crystal structure accepting $\text{Fe}^{3+}/\text{Fe}^{4+}$ state [6,8].

An additional information about local symmetry of Fe was obtained from Fe K-edge XANES. In 3d metals, the pre-edge feature in the K-edge range is attributed to the s-d quadrupole transition due to d-p mixing. The pre-edge peaks provides information about oxidation state and the local coordination geometry of the metal atom (e.g. tetrahedral versus octahedral) [46,47]. The inset in Fig. 4(a) shows a comparison of STO-Fe2e16-350 spectrum with the spectra of Fe_2O_3 standard and results of FEFF9 calculation for SrFeO_3 , $\text{Sr}_8\text{Fe}_8\text{O}_{23}$, $\text{Sr}_8\text{Ti}_5\text{Fe}_3\text{O}_{23}$, and $\text{Sr}_8\text{Ti}_3\text{Fe}_5\text{O}_{23}$ supercells. The presence of a pre-edge peak clearly indicates that iron is oxidized in STO-Fe2e16-350 sample. However, the peak is much more intense than in Fe_2O_3 standard spectrum, and its position is shifted to lower energy as compared with Fe_2O_3 . It showed that the local symmetry of Fe in STO-Fe2e16-350 sample differed from that of Fe_2O_3 . The position of the pre-edge feature in experimental spectrum of STO-Fe2e16-350 better conformed to iron rich phase $\text{Sr}_8\text{Ti}_3\text{Fe}_5\text{O}_{23}$. However its intensity is lower, which presents the evidence that the Fe sites of STO-Fe2e16-350C increasingly deviate from the centrosymmetric O_h geometry [47,48].

Further simulations were conducted to estimate the radial distribution of the nearest neighbors around Fe ion in STO-Fe2e16-350 sample. In the simulated supercells Fe was placed in either Ti or Sr site. Remarkable, the FEFF9 calculation showed that substitution of Fe in Sr site with the presence of oxygen vacancies provides better matching with the FT of experimental EXAFS data as shown in Fig. 5. The results imply that when there is a deficit of Sr in STO crystal, Fe can substitute both Ti and Sr sites. The situation is different from powder samples, where Fe tends to substitute Ti resulting in $\text{SrTi}_{1-x}\text{Fe}_x\text{O}_{3-\delta}$ mixed oxide compounds [6,8]. Our results for Fe ion implanted STO crystals suggest formation of $\text{Sr}_{1-y}\text{Ti}_{1-x}\text{Fe}_{x+y}\text{O}_{3-\delta}$ phase throughout entire Fe implanted layer. This phase is observed in RBS as Sr depleted area. However, the corresponding depletion of Ti content cannot be detected in RBS spectra, because Ti peak is lower in energy and mixed with signals from other elements (Fig. 1).

5. Conclusions

Strontium titanate single crystals were implanted with 30 keV Fe ion at several doses in the range from 2×10^{14} to 2×10^{16} ion/cm² and then annealed in oxygen atmosphere at 350 °C. The implantation resulted in structural disordering, and also, in depletion of Sr content which was observed in all implanted samples as evident from RBS analysis. Post-implantation anneal-

ing induced recrystallization and caused Fe incorporation into the host crystal structure. The ion irradiation induced defects increased STO surface reactivity with the gases from the ambient environment. In the presence of carbon contamination it led to formation of strontium carbonate on the surface of Fe implanted, and implanted and O₂ annealed STO samples. The oxidation state of Fe changed from Fe⁰ in as-implanted STO to Fe³⁺/Fe²⁺ in implanted and oxygen annealed STO samples. The FEFF9 calculation implied that Fe can substitute for both Ti sites and Sr sites forming Sr_{1-y}Ti_{1-x}Fe_{x+y}O_{3-δ} phase in O₂ annealed Fe-implanted STO samples.

Acknowledgements

This research was supported by the National Science and Engineering Research Council of Canada, the Canadian Foundation for Innovation, Canada Research Chairs (TKS) and the Ontario Ministry of Innovation. We would like to thank Jack Hendricks (Tandetron facility at the University of Western Ontario) for his help with fabrication of the samples, Mark Biesinger (Surface Science Western) for the assistance with XPS analysis, and Robert Gordon (Advanced Photon Source of Argonne National Laboratory and Canadian Light Source) for XANES measurements. We also thank Himasha Medhavi Wijesekara and Jeff Hutter for assistance with AFM analysis.

References

- [1] W. Meneskou, H.J. Schreiner, K.H. Hardtl, E. Ivers-Tiffee, *Sens. Actuators B: Chem.* 59 (2–3) (1999) 184–189.
- [2] A. Rothschild, S.J. Litzelman, H.L. Tuller, W. Meneskou, T. Schneider, E. Ivers-Tiffee, *Sens. Actuators B: Chem.* 108 (1–2) (2005) 223–230.
- [3] J.R. Jurado, F.M. Figueiredo, B. Gharbage, J.R. Frade, *Solid State Ionics* 118 (1–2) (1999) 89–97.
- [4] S. Steinsvik, R. Bugge, J. Gjones, J. Tafto, T. Norby, *J. Phys. Chem. Solids* 58 (6) (1997) 969–976.
- [5] A. Rothschild, W. Meneskou, H.L. Tuller, E. Ivers-Tiffee, *Chem. Mater.* 8 (16) (2006) 3651–3659.
- [6] Y. Takeda, K. Kanno, T. Takada, O. Yamamoto, M. Takano, N. Nakayama, Y. Bando, *J. Solid State Chem.* 63 (1986) 237–249.
- [7] A. Sendilkumar, P.D. Babu, M.M. Raja, V.R. Reddy, A. Gupta, S. Srinath, *J. Am. Ceram. Soc.* 96 (9) (2013) 2973–2978.
- [8] M. Vrancar, A. Kuzmin, R. Merkle, J. Purans, E.A. Kotomin, J. Maier, O. Mathon, *Phys. Rev. B* 76 (17) (2007) 174107.
- [9] F.A. Kroger, H.J. Vink, *Solid State Phys.* 3 (1956) 307–435.
- [10] E. Bakken, N.L. Allan, T.H.K. Barron, C.E. Mohn, I.T. Todorov, S. Stolen, *Phys. Chem. Chem. Phys.* 5 (11) (2003) 2237–2243.
- [11] F. Voigts, C. Argirakis, W. Maus-Friedrichs, *Surf. Interface Anal.* 43 (6) (2011) 984–992.
- [12] F. Voigts, C. Argirakis, W. Maus-Friedrichs, *Surf. Interface Anal.* 44 (3) (2012) 301–307.
- [13] R. Merkle, J. Maier, *Angew. Chem. Int. Ed.* 47 (21) (2008) 3874–3894.
- [14] K. Sahner, R. Moos, M. Matam, J.J. Tunney, M. Post, *Sens. Actuators B: Chem.* 108 (1–2) (2005) 102–112.
- [15] X. Wei, G. Xu, Z.H. Ren, C.X. Xu, W.J. Weng, G. Shen, G.R. Han, *J. Am. Ceram. Soc.* 93 (5) (2010) 1297–1305.
- [16] D.P. Fagg, V.V. Kharton, A.V. Kovalevsky, A.P. Viskup, E.N. Naumovich, J.R. Frade, *J. Eur. Ceram. Soc.* 21 (10–11) (2001) 1831–1835.
- [17] N.Q. Minh, *J. Am. Ceram. Soc.* 76 (3) (1993) 563–588.
- [18] A.L. Shaula, V.V. Kharton, M.V. Patrakeev, J.C. Waerenborgh, D.P. Rojas, F.M.B. Marques, *Ionics* 10 (5–6) (2004) 378–384.
- [19] A. Beck, J.G. Bednorz, Ch. Gerber, C. Rosseel, D. Widmer, *Appl. Phys. Lett.* 77 (1) (2000) 139–141.
- [20] M. Janousch, G.I. Meijer, U. Staub, B. Delley, S.F. Karg, B.P. Andreasson, *Adv. Mater.* 19 (17) (2007) 2232–2235.
- [21] R. Waser, R. Dittmann, G. Staikov, K. Szot, *Adv. Mater.* 21 (25–26) (2009) 2632–2663.
- [22] D. Choudhury, S. Mukherjee, P. Mandal, A. Sundaresan, U.V. Waghmare, S. Bhattacharjee, R. Mathieu, P. Lazor, O. Eriksson, B. Sanyal, P. Nordblad, A. Sharma, S.V. Bhat, O. Karis, D.D. Sarma, *Phys. Rev. B* 84 (12) (2011) 125124.
- [23] X. Yang, T.Y. Liu, Z.J. Cheng, H.X. Gan, J.Y. Chen, *Physica B* 407 (5) (2012) 844–848.
- [24] M. Valant, T. Kolodiaznyi, I. Arcon, F. Aguesse, A.-K. Axelsson, N.M. Alford, *Adv. Funct. Mater.* 22 (10) (2012) 2114–2122.
- [25] E.N. Dulov, N.G. Ivoilov, O.A. Streibkov, L.R. Tagirov, V.I. Nuzhdin, R.I. Khaibullin, S. Kazan, F.A. Mikailzade, *Mater. Res. Bull.* 46 (12) (2011) 2304–2307.
- [26] J. Leveneur, G.I.N. Waterhouse, J. Kennedy, J.B. Metson, D.R.G. Mitchell, *J. Phys. Chem. C* 115 (43) (2011) 20978–20985.
- [27] S.Q. Zhou, K. Potzger, Q.Y. Xu, K. Kuepper, G. Talut, D. Marko, A. Mucklich, M. Helm, J. Fassbender, E. Arenholz, H. Schmidt, *Phys. Rev. B* 80 (9) (2009) 094409.
- [28] M. Mayer, *SIMNRA User's Guide*, Max-Planck-Institut für Plasmaphysik, Garching, Germany, 1997.
- [29] M.C. Biesinger, L.W.M. Lau, A.R. Gerson, R.S.C. Smart, *Appl. Surf. Sci.* 257 (3) (2010) 887–898.
- [30] M.C. Biesinger, B.P. Payne, A.P. Grosvenor, L.W.M. Lau, A.R. Gerson, R.S. Smart, *Appl. Surf. Sci.* 257 (7) (2011) 2717–2730.
- [31] D. Wagner, A.V. Naumkin, A. Kraut-Vass, J.W. Allison, C.J. Powell, J.R. Rumble Jr., *NIST* (2003).
- [32] N. Fairley, *CasaXPS* (2005).
- [33] J.J. Rehr, J.J. Kas, M.P. Prange, A.P. Sorini, Y. Takimoto, F. Vila, *C. R. Phys.* 10 (6) (2009) 548–559.
- [34] J.J. Rehr, J.J. Kas, F.D. Vila, M.P. Prange, K. Jorissen, *Phys. Chem. Chem. Phys.* 12 (21) (2010) 5503–5513.
- [35] M.E. Pilleux, C.R. Grahmann, V.M. Fuenzalida, *J. Am. Ceram. Soc.* 77 (6) (1994) 1601–1604.
- [36] S. Bhaskar, D. Allgeyer, J.A. Smythe, *Appl. Phys. Lett.* 89 (25) (2006) 254103.
- [37] J.D. Baniecki, M. Ishii, K. Kurihara, K. Yamanaka, T. Yano, K. Shinozaki, T. Imada, K. Nozaki, N. Kin, *Phys. Rev. B* 78 (19) (2008) 195415.
- [38] H.N. Lee, H.M. Christen, M.F. Chisholm, C.M. Rouleau, D.H. Lowndes, *Appl. Phys. Lett.* 84 (2004) 4107–4109.
- [39] S. Azad, M.H. Engelhard, L.Q. Wang, *J. Phys. Chem. B* 109 (20) (2005) 10327–10331.
- [40] P.A.W. van der Heide, Q.D. Jiang, Y.S. Kim, J.W. Rabalais, *Surf. Sci.* 473 (1–2) (2001) 59–70.
- [41] K. Szot, W. Speier, U. Breuer, R. Meyer, J. Szade, R. Waser, *Surf. Sci.* 460 (1–3) (2000) 112–128.
- [42] J. Shin, S.V. Kalinin, H.N. Lee, H.M. Christen, R.G. Moore, E.W. Plummer, A.P. Baddorf, *J. Mater. Res.* 19 (12) (2004) 3447–3450.
- [43] C. Sabathier, J. Chaumont, S. Rouziere, A. Traverse, *Nucl. Instrum. Methods Phys. Res. Sect. B: Beam Interact. Mater. Atoms* 234 (4) (2005) 509–519.
- [44] Y. Chen, W. Jung, Z.H. Cai, J.J. Kim, H.L. Tuller, B. Yildiz, *Energy Environ. Sci.* 5 (7) (2012) 7979–7988.
- [45] L.V. Goncharova, D.G. Starodub, E. Garfunkel, T. Gustafsson, V. Vaithyanathan, J. Lettieri, D.G. Schlom, *J. Appl. Phys.* 100 (1) (2006) 014912.
- [46] M.F. de Groot, 14th International Conference on X-Ray Absorption Fine Structure (XAFS14) Proceedings 190 (2009) 012004.
- [47] T.E. Westre, P. Kennepohl, J.G. DeWitt, B. Hedman, K.O. Hodgson, E.I. Solomon, *J. Am. Chem. Soc.* 119 (27) (1997) 6297–6314.
- [48] L.X. Chen, T. Liu, M.C. Thurnauer, R. Csencsits, T. Rajh, *J. Phys. Chem. B* 106 (34) (2002) 8539–8546.